symmetry

MDPI

Article

Controlling Achiral and Chiral Properties with an Electric Field: A Next-Generation QTAIM Interpretation

Wenjing Yu [1], Zi Li [1], Yuting Peng [1], Xinxin Feng [1], Tianlv Xu [1], Herbert Früchtl [2], Tanja van Mourik [2], Steven R. Kirk [1,*] and Samantha Jenkins [1,*]

[1] Key Laboratory of Chemical Biology and Traditional Chinese Medicine Research and Key Laboratory of Resource, National and Local Joint Engineering Laboratory for New Petro-chemical Materials and Fine Utilization of Resources, College of Chemistry and Chemical Engineering, Hunan Normal University, Changsha 410081, China

[2] EaStCHEM School of Chemistry, University of Saint Andrews, North Haugh, St Andrews, Fife KY16 9ST, UK

* Correspondence: steven.kirk@cantab.net (S.R.K.); samanthajsuman@gmail.com (S.J.)

Abstract: We used the recently introduced stress tensor trajectory U_σ space construction within the framework of next-generation quantum theory of atoms in molecules (NG-QTAIM) for a chirality investigation of alanine when subjected to a non-structurally distorting electric field. The resultant sliding of the axial-bond critical point (*BCP*) responded significantly, up to twice as much, in the presence of the applied electric field in comparison to its absence. The bond flexing, a measure of bond strain, was always lower by up to a factor of four in the presence of the electric field, depending on its direction and magnitude. An achiral character of up to 7% was found for alanine in the presence of the applied electric field. The achiral character was entirely absent in the presence of the lowest value of the applied electric field. Future applications, including molecular devices using left and right circularly polarized laser pulses, are briefly discussed.

Keywords: Next Generation QTAIM; alanine; electric field

Citation: Yu, W.; Li, Z.; Peng, Y.; Feng, X.; Xu, T.; Früchtl, H.; van Mourik, T.; Kirk, S.R.; Jenkins, S. Controlling Achiral and Chiral Properties with an Electric Field: A Next-Generation QTAIM Interpretation. *Symmetry* **2022**, *14*, 2075. https://doi.org/10.3390/sym14102075

Academic Editor: Enrico Bodo

Received: 12 September 2022
Accepted: 3 October 2022
Published: 6 October 2022

Publisher's Note: MDPI stays neutral with regard to jurisdictional claims in published maps and institutional affiliations.

1. Introduction

Chirality is widely observed in nature and is definable as the geometric property of a molecule, where its mirror image is non-superimposable. Enantiomers are the left- and right-handed forms of chiral molecules that possess identical chemical properties when using scalar chemical measures but may demonstrate strong enantiomeric preference during chemical reactions. The development of reliable methods to discern enantiomers has received considerable attention in recent years [1].

Some of the current authors recently used NG-QTAIM to quantify a chirality-helicity measure [2], which is an association between molecular chirality and helical characteristics known as the chirality-helicity equivalence, first described by Wang [3], and is consistent with photoexcitation circular dichroism experiments [4]. Wang hypothesized that the origin of the helical characteristic was not attributable to steric hindrance or molecular geometries alone but required insight derived from the electronic structure. Recently, the interdependence of steric and electronic factors was discovered to be more complex [5] than discernable from the molecular geometries associated with the helical electronic transitions of spiro-conjugated molecules [6,7]. Enantiomers of isolated molecules or molecules during reactions can, however, be distinguished using the vector-based chemical measures that are used in next-generation QTAIM (NG-QTAIM) [8].

Previously [2], we established the presence of a distinct helical-shaped stress tensor trajectory $T_\sigma(s)$ for lactic acid and alanine. If the value of the chirality $C_\sigma > 0$, and the value

is larger for the CCW than for the CW directions of the torsion angle θ, a preference is indicated for $\mathbf{S}_\sigma$ compared to $\mathbf{R}_\sigma$ stereoisomers in U_σ space; see the Theoretical Background and Computational Details section. The $\mathbf{S}_\sigma$ and $\mathbf{R}_\sigma$ chirality assignments for lactic acid and alanine were in full agreement with the Cahn–Ingold–Prelog (CIP) priority rules [9]. Later, we developed the NG-QTAIM interpretation of chirality by quantifying the chirality-helicity equivalence by formulating the chirality-helicity function $C_{helicity}$ [7,8,10]. This previous work, however, was limited by the use of only a single dihedral angle to construct $T_\sigma(s)$, which consequently did not fully sample the bonding environment of the chiral carbon (C1). This limitation has been recently addressed using the new *spanning* $T_\sigma(s)$ [11] for (achiral) singly halogen (F, Cl or Br) substituted and (chiral) doubly halogen substituted ethane. We also used the spanning $T_\sigma(s)$ to construct the chirality-helicity function $C_{helicity}$ to demonstrate the NG-QTAIM interpretation of achiral behavior: $C_{helicity}$ = 0 comprised an equal and cancelling mix of $\mathbf{S}_\sigma$ and $\mathbf{R}_\sigma$ stereoisomer contributions in U_σ space. This was also discovered for ethane [12]. We found that within NG-QTAIM, formally achiral molecules may contain chiral contributions but these summed to zero when using the spanning form of the $T_\sigma(s)$.

An enhanced ability of tracking changes to the chirality and the ability to distinguish enantiomers during the course of a reaction when subjected to an electric (**E**) field is vital to a wide range of sciences. For instance, Shaik et al. recently investigated an **E** field for use as a 'smart reagent' for the control of the reactivity and structure for chemical catalysis in a range of reactions [13].

Recently, we examined formally achiral glycine subjected to an **E** field [14] using NG-QTAIM. This work followed on from investigations performed by Wolk et al. on the application of an **E** field to induce stereoisomers via symmetry breaking changes to the length of the C-H bonds [15]. Again, this previous study on glycine was unable to provide the mix of $\mathbf{S}_\sigma$ and $\mathbf{R}_\sigma$ stereoisomer contributions in U_σ space for each of the S_a and R_a geometric stereoisomers due to the use of only a single dihedral angle to construct $T_\sigma(s)$.

The construction of the *spanning* $T_\sigma(s)$ enables the determination of the degree of mixing of $\mathbf{S}_\sigma$ and $\mathbf{R}_\sigma$ stereoisomers that may occur when alanine is subjected to an **E** field, as shown in Scheme 1.

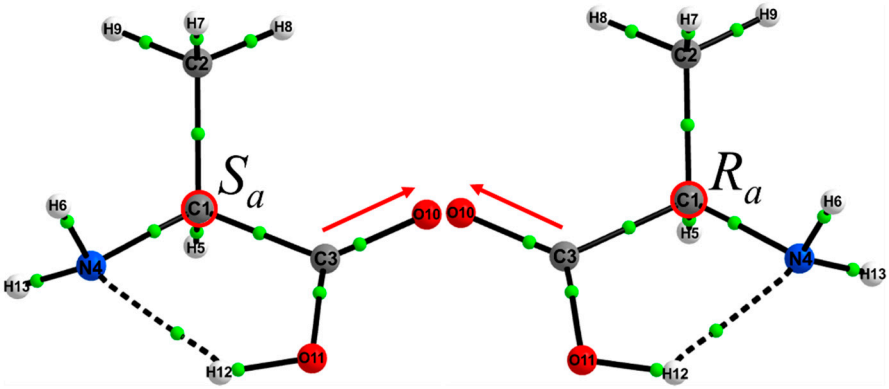

Scheme 1. Molecular graphs of the S_a stereoisomer (left panel) and R_a stereoisomer (right panel) of alanine. The green spheres indicate the bond critical points (*BCP*s). The red arrows indicate the directions of the positive (+**E**) field along the C3→O10 *BCP* bond path and negative (-**E**) field along the C3←O10 *BCP* bond path. The C3, N4, and H5 atoms are bonded to the C1 atom; the H6, H7, and H8 atoms are bonded to the C2 atom. Numbered atoms in black define the dihedral angles {(3127, 3128, 3129), (4127, 4128, 4129), and (5127, 5128, 5129)} used in the construction of the spanning stress tensor trajectory $T_\sigma(s)$; see the Computational Details section.

A goal of this investigation was to understand the consequences of any mixing of the $\mathbf{S}_\sigma$ and $\mathbf{R}_\sigma$ stereoisomers that may occur when alanine is subjected to a non-structurally distorting **E** field, since $\mathbf{S}_\sigma$ and $\mathbf{R}_\sigma$ mixing indicates the presence of an achiral character. Another goal was to test the effect of the **E** fields on the chirali-

ty-helicity function $C_{helicity}$ of alanine, the NG-QTAIM interpretation of chirality, along the C3→O10 *BCP* bond path and the C3←O10 *BCP* bond path attached to the chiral carbon (C1), as shown in Scheme 1. We used the **E** fields: ±25 × 10^{-4} a.u., ±50 × 10^{-4} a.u., and ±100 × 10^{-4} a.u., which are experimentally accessible, using a scanning tunneling microscope (STM).

2. Theoretical Background

The background of QTAIM and next-generation QTAIM (NG-QTAIM), including the procedure used to generate the stress tensor trajectories $T_\sigma(s)$, is provided in the Supplementary Materials S1. The ellipticity, ε, quantifies the relative accumulation of the electronic charge density $\rho(\mathbf{r_b})$ distribution in the two directions perpendicular to the bond path at a bond critical point (*BCP*) with position $\mathbf{r_b}$. For values of the ellipticity $\varepsilon > 0$ and where the ellipticity $\varepsilon \neq 0$, the shortest and longest axes of the elliptical distribution of $\rho(\mathbf{r_b})$ are associated with the λ_1 and λ_2 eigenvalues, respectively, and the ellipticity is defined as $\varepsilon = \lambda_1/\lambda_2 - 1$. Note that λ_1 and λ_2 both possess negative signs, where $\lambda_1 \leq \lambda_2 < \lambda_3$ and $\lambda_3 > 0$.

We used the Bader's formulation of the quantum stress tensor $\boldsymbol{\sigma}(\mathbf{r})$ [16] to quantify the mechanics of the forces that act on the electron density distribution in open systems defined by:

$$\boldsymbol{\sigma}(\mathbf{r}) = -\frac{1}{4}\left[\left(\frac{\partial^2}{\partial \mathbf{r}_i \partial \mathbf{r}'_j} + \frac{\partial^2}{\partial \mathbf{r}'_i \partial \mathbf{r}_j} - \frac{\partial^2}{\partial \mathbf{r}_i \partial \mathbf{r}_j} - \frac{\partial^2}{\partial \mathbf{r}'_i \partial \mathbf{r}'_j}\right) \cdot \gamma(\mathbf{r}, \mathbf{r}')\right]_{\mathbf{r}=\mathbf{r}'} \quad (1)$$

where $\gamma(\mathbf{r},\mathbf{r}')$ is the one-body density matrix:

$$\gamma(\mathbf{r}, \mathbf{r}') = N \int \Psi(\mathbf{r}, \mathbf{r}_2, \ldots, \mathbf{r}_N)\Psi^*(\mathbf{r}', \mathbf{r}_2, \ldots, \mathbf{r}_N)\mathrm{d}\mathbf{r}_2 \cdots \mathrm{d}\mathbf{r}_N \quad (2)$$

The stress tensor is any quantity $\boldsymbol{\sigma}(\mathbf{r})$ that satisfies Equation (2) since any divergence-free tensor can be added to the stress tensor while satisfying this definition [16–18]. Bader's formulation of the stress tensor [16], Equation (1), is used in the AIMAll QTAIM package [19] and in this investigation due to the superior performance of the stress tensor compared with the Hessian of $\rho(\mathbf{r})$ for more clearly distinguishing the R_a and S_a stereoisomers of lactic acid and alanine [20]. Earlier, we demonstrated that the most and least preferred directions for bond displacement correspond to the most and least preferred direction of $\rho(\mathbf{r})$ displacement, respectively, namely the $\mathbf{e}_{1\sigma}$ and $\mathbf{e}_{2\sigma}$ eigenvectors, respectively, of the stress tensor [8].

The chirality C_σ is quantified by the bond torsion direction CCW vs. CW, where the largest magnitude stress tensor eigenvalue ($\lambda_{1\sigma}$) is associated with $\mathbf{e}_{1\sigma}$**.** The stress tensor $\boldsymbol{\sigma}(\mathbf{r})$ eigenvector $\mathbf{e}_{1\sigma}$ corresponds to the direction in which the electrons at the C1-C2 *BCP* are subject to the most compressive forces. Therefore, $\mathbf{e}_{1\sigma}$ corresponds to the direction along which the C1-C2 *BCP* electrons will be most displaced when the C1-C2 *BCP* is subjected to torsion [21]. The chirality C_σ for each dihedral angle is defined as the difference in the maximum projections: the dot product of the stress tensor $\mathbf{e}_{1\sigma}$ eigenvector and the *BCP* displacement **dr** of the $T_\sigma(s)$ values between the CCW and CW torsion θ is defined as:

$$C_\sigma = [(\mathbf{e}_{1\sigma} \cdot \mathbf{dr})_{max}]_{CCW} - [(\mathbf{e}_{1\sigma} \cdot \mathbf{dr})_{max}]_{CW} \quad (3)$$

The bond flexing F_σ, defined as:

$$F_\sigma = [(\mathbf{e}_{2\sigma} \cdot \mathbf{dr})_{max}]_{CCW} - [(\mathbf{e}_{2\sigma} \cdot \mathbf{dr})_{max}]_{CW} \quad (4)$$

The bond flexing F_σ, see Equation (4), provides a measure of the 'flexing-strain' of a bond path for each dihedral angle, which is particularly of use when a molecule is subjected to an **E** field.

The bond axiality A_σ for each dihedral angle provides a measure of the chiral asymmetry, defined as:

$$A_\sigma = [(\mathbf{e}_{3\sigma}\cdot\mathbf{dr})_{max}]_{CCW} - [(\mathbf{e}_{3\sigma}\cdot\mathbf{dr})_{max}]_{CW} \quad (5)$$

The bond axiality A_σ, see Equation (5), quantifies the direction of *axial* displacement of the bond critical point (*BCP*) in response to the bond torsion (CCW vs. CW), i.e., the sliding of the *BCP* along the bond path [22]**.** The (±) sign of the chirality C_σ, see Equation (3). bond flexing F_σ, and bond axiality A_σ determine the prevalence of the $\mathbf{S}_\sigma$ ($C_\sigma > 0$, $F_\sigma > 0$, $A_\sigma > 0$) or $\mathbf{R}_\sigma$ ($C_\sigma < 0$, $F_\sigma < 0$, $A_\sigma < 0$) character, as shown in Table 1. For formally achiral molecules, we may define an additional null-chirality assignment $\mathbf{Q}_\sigma$ (≈ 0 chiral character) that occurs for the ethane molecule [12] and singly halogen substituted ethane [11]. The ± sign, however, is not used with the assignment $\mathbf{Q}_\sigma$ as it is for the $\mathbf{S}_\sigma$ and $\mathbf{R}_\sigma$ assignments since $C_\sigma = 0$, $F_\sigma = 0$, and $A_\sigma = 0$ in this case.

Table 1. The variation of the total U_σ space distortion set ∑{chirality C_σ, bond flexing F_σ, bond axiality A_σ} with the **E** field of the $\mathbf{S}_\sigma$ and $\mathbf{R}_\sigma$ components for the S_a and R_a geometric stereoisomers. The contributions from the nine dihedral angles used for the construction of $T_\sigma(s)$ are provided in the Supplementary Materials S5, see Scheme 1 as well. The sums of the corresponding mixing ratios are defined as $C_{\sigma mixing} = \sum_{S\sigma}\{C_\sigma\}/|\sum_{R\sigma}\{C_\sigma\}|$, $F_{\sigma mixing} = \sum_{S\sigma}\{F_\sigma\}/|\sum_{R\sigma}\{F_\sigma\}|$, and $A_{\sigma mixing} = \sum_{S\sigma}\{A_\sigma\}/|\sum_{R\sigma}\{A_\sigma\}|$.

	S_a	R_a			
(±)E-field × 10^{-4} au	**∑{C_σ, F_σ, A_σ}**	**∑{C_σ, F_σ, A_σ}**	**$C_{\sigma mixing}$**	**$F_{\sigma mixing}$**	**$A_{\sigma mixing}$**
0	{4.1229**[$\mathbf{S}_\sigma$]**, −4.0252**[$\mathbf{R}_\sigma$]**, −0.2815**[$\mathbf{R}_\sigma$]**}	{−4.1230**[$\mathbf{R}_\sigma$]**, 4.0254**[$\mathbf{S}_\sigma$]**, 0.2792**[$\mathbf{S}_\sigma$]**}	0.0226	0.0000	0.0000
−25	{2.9650**[$\mathbf{S}_\sigma$]**, −2.6204**[$\mathbf{R}_\sigma$]**, −0.4810**[$\mathbf{R}_\sigma$]**}	{−2.9635**[$\mathbf{R}_\sigma$]**, 2.6176**[$\mathbf{S}_\sigma$]**, 0.4815**[$\mathbf{S}_\sigma$]**}	0.0000	0.0507	0.0000
−50	{3.2299**[$\mathbf{S}_\sigma$]**, −0.9131**[$\mathbf{R}_\sigma$]**, −0.4853**[$\mathbf{R}_\sigma$]**}	{−3.2299**[$\mathbf{R}_\sigma$]**, 0.9131**[$\mathbf{S}_\sigma$]**, 0.4855**[$\mathbf{S}_\sigma$]**}	0.0671	0.2927	0.0000
−100	{3.0467**[$\mathbf{S}_\sigma$]**, −1.2629**[$\mathbf{R}_\sigma$]**, −0.4664**[$\mathbf{R}_\sigma$]**}	{−3.0464**[$\mathbf{R}_\sigma$]**, 1.2629**[$\mathbf{S}_\sigma$]**, 0.4660**[$\mathbf{S}_\sigma$]**}	0.0697	0.1654	0.0000
+25	{3.3800**[$\mathbf{S}_\sigma$]**, −2.5347**[$\mathbf{R}_\sigma$]**, −0.4756**[$\mathbf{R}_\sigma$]**}	{−3.3812**[$\mathbf{R}_\sigma$]**, 2.5328**[$\mathbf{S}_\sigma$]**, 0.4752**[$\mathbf{S}_\sigma$]**}	0.0000	0.0619	0.0000
+50	{3.8112**[$\mathbf{S}_\sigma$]**, −1.0034**[$\mathbf{R}_\sigma$]**, −0.5104**[$\mathbf{R}_\sigma$]**}	{−3.8113**[$\mathbf{R}_\sigma$]**, 1.0036**[$\mathbf{S}_\sigma$]**, 0.5108**[$\mathbf{S}_\sigma$]**}	0.0387	0.2947	0.0000
+100	{4.3111**[$\mathbf{S}_\sigma$]**, −0.9069**[$\mathbf{R}_\sigma$]**, −0.5638**[$\mathbf{R}_\sigma$]**}	{−4.3111**[$\mathbf{R}_\sigma$]**, 0.9071**[$\mathbf{S}_\sigma$]**, 0.5642**[$\mathbf{S}_\sigma$]**}	0.0202	0.3232	0.0000

We include all the contributions to the U_σ space chirality from the 'chiral' center C1 of alanine. This is undertaken by constructing all nine torsion C1-C2 *BCP* $T_\sigma(s)$ that use dihedral angles that include the C1 atom, see Scheme 1. We refer to this process of using all nine torsion C1-C2 *BCP* $T_\sigma(s)$ as the so-called *spanning* U_σ space chirality construction. The result of this process is a complete set of alanine U_σ space isomers, with possible chirality assignments $\mathbf{Q}_\sigma$, $\mathbf{S}_\sigma$, or $\mathbf{R}_\sigma$. The linear sum of the individual components of the symmetry inequivalent U_σ space distortion sets ∑{C_σ,F_σ,A_σ} is calculated.

The chirality-helicity function $C_{helicity}$ (=$C_\sigma|A_\sigma|$) summed over each of the dihedral angles used to construct the $T_\sigma(s)$ is required to determine whether a molecule is formally achiral. We tabulate $C_{helicity}$ in the absence of an applied **E** field and refer to this as $C_{helicity\mathbf{E}} = C_{\sigma\mathbf{E}}|A_{\sigma\mathbf{E}}$, which is the product of the ratio of the chirality $C_{\sigma\mathbf{E}} = \sum C_\sigma/\sum C_\sigma|_{E=0}$ and the ratio of the bond axiality $A_{\sigma\mathbf{E}} = \sum A_\sigma/\sum A_\sigma|_{E=0}$, see Table 2. Ethane, for instance, comprises $C_{helicity}$ values: $\mathbf{Q}_\sigma$ (=0), $\mathbf{S}_\sigma$ (=+0.0003), and $\mathbf{R}_\sigma$ (=−0.0003), which sum to give $\sum C_{helicity} = 0$. The chirality C_σ is formed from the $\underline{\mathbf{e}}_{1\sigma}\cdot\mathbf{dr}$ (bond twist) *BCP* shift in the plane perpendicular to $\underline{\mathbf{e}}_{3\sigma}$ (the bond path). The axiality A_σ is formed from the axial *BCP* sliding $\mathbf{e}_{3\sigma}\cdot\mathbf{dr}$ (bond axiality) [22], where the *BCP* sliding is the shift of the *BCP* position along the containing bond path due to changes in the bonded inter-nuclear separations.

Table 2. The variation of the chirality C_σ, bond flexing F_σ, and bond axiality A_σ with the ±**E** field specified by the ratios $C_{\sigma\mathbf{E}} = \sum C_\sigma / \sum C_\sigma|_{\mathbf{E}=0}$, $F_{\sigma\mathbf{E}} = \sum F_\sigma / \sum F_\sigma|_{\mathbf{E}=0}$, and $A_{\sigma\mathbf{E}} = \sum A_\sigma / \sum A_\sigma|_{\mathbf{E}=0}$ of the S_a and R_a stereoisomers of alanine. The chirality-helicity function $\sum C_{helicity}$ is presented for the S_a stereoisomer. $C_{helicity\mathbf{E}}$ is defined by the product $C_{\sigma\mathbf{E}}|A_{\sigma\mathbf{E}}|$, where the value of $\sum C_{helicity\mathbf{E}=0} = 1.1604$, i.e., in the absence of an **E** field.

	S_a			R_a			
(±)E-field × 10^{-4} au	$\mathbf{C_{\sigma E}}$	$\mathbf{F_{\sigma E}}$	$\mathbf{A_{\sigma E}}$	$\mathbf{C_{\sigma E}}$	$\mathbf{F_{\sigma E}}$	$\mathbf{A_{\sigma E}}$	$\mathbf{C_{helicity E}}$
−25	0.7192	0.6510	1.7087	0.7188	0.6503	1.7246	1.2291
−50	0.7834	0.2268	1.7240	0.7834	0.2268	1.7389	1.3509
−100	0.7390	0.3137	1.6568	0.7389	0.3137	1.6691	1.2245
+25	0.8198	0.6297	1.6895	0.8201	0.6292	1.7020	1.3852
+50	0.9244	0.2493	1.8131	0.9244	0.2493	1.8295	1.6764
+100	1.0456	0.2253	2.0028	1.0456	0.2253	2.0208	2.0947

In this investigation, the presence of a mix of $\mathbf{S}_\sigma$ and $\mathbf{R}_\sigma$ chirality assignments for the components of the S_a or R_a geometric stereoisomers of alanine are referred to as *mixed* chirality C_σ in U_σ space and are determined by a value of $C_{\sigma mixing} = \sum \mathbf{S}_\sigma\{C_\sigma\} / |\sum \mathbf{R}_\sigma\{C_\sigma\}| > 0$. Earlier, an equal mixing of the $\mathbf{S}_\sigma$ and $\mathbf{R}_\sigma$ chirality was found for the formally achiral ethane [12] and corresponds to the maximum value possible $C_{\sigma mixing} = 1$. We consider the degree of mixing of the chirality $C_{\sigma mixing} = \sum \mathbf{S}_\sigma\{C_\sigma\} / |\sum \mathbf{R}_\sigma\{C_\sigma\}|$, the bond flexing $F_{\sigma mixing} = \sum \mathbf{S}_\sigma\{F_\sigma\} / |\sum \mathbf{R}_\sigma\{F_\sigma\}|$, and bond axiality $A_{\sigma mixing} = \sum \mathbf{S}_\sigma\{A_\sigma\} / |\sum \mathbf{R}_\sigma\{A_\sigma\}|$, where all are bounded by the limits [0, 1]. Values of $A_{\sigma mixing} = 0$ would occur in instances of insignificant torsional C1-C2 *BCP* bond path curvature since the eigenvector $\mathbf{e}_{3\sigma}$, which is directed along the bond path ($\boldsymbol{r}$), is always perpendicular to the plane defined by the eigenvectors $\mathbf{e}_{1\sigma}$ and $\mathbf{e}_{2\sigma}$**.** The presence of non-zero bond path curvature is determined by a non-zero difference of the bond path length (BPL) and the geometric separation (GBL) of the pair of bonded nuclei, as shown in the Supplementary Materials S2.

Computational Details

The alanine molecular geometry was initially optimized with the 'verytight' convergence criteria with the B3LYP/cc-pVQZ level of DFT theory using Gaussian 09.E01 [23] and employing an 'ultrafine' integration grid. The wavefunctions were converged to less than 10^{-10} RMS change in the density matrix and less than 10^{-8} maximum change in the density matrix. All the subsequent **E** field optimization, torsion, and single-point steps then used identical convergence criteria. An iterative process is used to create the **E**-field-induced isomers. This was undertaken by directing an **E** field parallel (+**E** field) or anti-parallel (-**E** field) to the C3-O10 *BCP* bond path, see Scheme 2.

Each of the S_a and R_a geometric stereoisomers were subjected to an iterative process consisting of two steps: Step (I): a molecule alignment step: the alpha C3 atom was fixed at the origin of the coordinate frame, whereas the selected C3-O10 bond was aligned along a reference axis with the positive direction of the axis from C3 to O10 and the C3 atom consistently aligned in the same plane. Step (II): a constrained optimization step with the selected **E** field directed along the reference axis. The sign convention by default G09 is for the **E** field relative to the reference axis used. This two-step process was repeated ten times to ensure the consistency of the **E** field application direction and the required bond (C3-O10) direction. The resulting molecular geometries were subsequently used in the torsion calculations, where the C3-O10 bond lengths were constrained to their **E**-field-optimized values. The alanine molecule was subjected to **E** fields = ±25 × 10^{-4} a.u., ±50 × 10^{-4} a.u., and ±100 × 10^{-4} a.u. before the molecule was torsioned to construct the trajectories $T_\sigma(s)$ from the series of rotational isomers $-180.0° \le \theta \le +180.0°$ for the torsional C1-C2 *BCP* of alanine. The direction of torsion is defined as CCW ($-180.0° \le \theta \le 0.0°$) or CW ($0.0° \le \theta \le +180.0°$) from a decrease or an increase in the dihedral angle, respectively, see Scheme 2. The $T_\sigma(s)$ for the complete set of nine ordered sets

of four atoms defines the dihedral angles: {(3127, 3128, 3129), (4127, 4128, 4129), (5127, 5128, 5129)}, which were calculated. See Scheme 1 for the dihedral atom numbering.

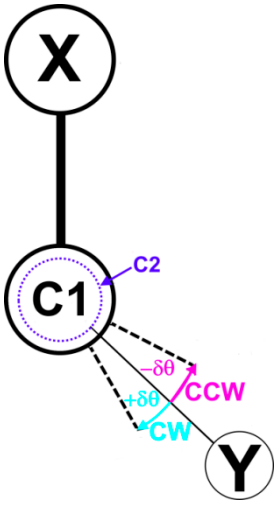

Scheme 2. Definition of clockwise (CW) and counter-clockwise (CCW) directions of torsion using the conventional geometric dihedral angle θ defined by the sequence of atoms X = {C3, N4, H5}, C1, C2, Y = {H7, H8, H9}, sequentially further away from the viewing plane perpendicular to the C1–C2 direction, with atom X closest to the viewer and in the "12 o'clock" position. A negative step (−δθ) in the dihedral angle θ corresponds to C2—Y rotating in a CCW direction in the viewing plane; conversely, a positive step (+δθ) in the dihedral angle θ corresponds to C2—Y rotating in a CW direction in the viewing plane.

Single-point calculations were undertaken on each torsion scan geometry where the SCF iterations converged to less than 10^{-10} RMS change in the density matrix and less than 10^{-8} maximum change in the density matrix to yield the final wavefunctions for the QTAIM and stress tensor $\boldsymbol{\sigma}(\mathbf{r})$, which was conducted using the AIMAll [19] and QuantVec [24] suite on each wavefunction, obtained in the previous step. All molecular graphs were confirmed to be free of non-nuclear attractor (*NNA*) critical points.

3. Results and Discussions

In this investigation, the scalar distance measures: geometric bond length (GBL) and bond path length (BPL), were not sufficient to quantify any chiral effects with or without the presence of an applied non-structurally distorting **E** field = ±25 × 10^{-4} a.u., ±50 × 10^{-4} a.u., and ±100 × 10^{-4} a.u. and are supplied in the Supplementary Materials S2. None of the torsional C1-C2 *BCP* bond path curvatures were significantly non-zero, see Supplementary Materials S2. The other scalar measures for alanine without and with an **E** field are supplied in the Supplementary Materials S3.

The stress tensor trajectories $T_\sigma(s)$ for the torsion C1-C2 *BCP* demonstrate the helical form that appears to be characteristic of chiral molecules, as shown in Figures 1–4, where the same axis scales are used throughout. This finding is consistent with the helical-shaped $T_\sigma(s)$ previously observed for the alanine C1-C2 *BCP* $T_\sigma(s)$, which were obtained using only a single dihedral angle [9].

The total $\mathbf{S}_\sigma$ and $\mathbf{R}_\sigma$ chirality assignments in U_σ space correspond to the S_a and R_a geometric stereoisomers, respectively, of alanine, fully consistent with the CIP priority rules, as shown in Table 1. The sets of nine components that comprise each C1-C2 *BCP* $T_\sigma(s)$ along with the intermediate results are provided in the Supplementary Materials S4. Inspection of the nine components of C1-C2 *BCP* $T_\sigma(s)$ demonstrates the presence of both $\mathbf{S}_\sigma$ and $\mathbf{R}_\sigma$ stereoisomers for each of the S_a and R_a geometric stereoisomers. This mix is quantified by $C_{\sigma mixing}$, $F_{\sigma mixing}$, and $A_{\sigma mixing}$; see the Background Theory section and Table

1. Without an applied **E** field, a degree of mixing of the **Sσ** and **Rσ** U_σ space chirality C_σ of the stereoisomers is apparent from the non-zero value of $C_{\sigma mixing}$.

The values of $C_{\sigma mixing} = 0$ indicate there was no mixing of the **Sσ** and **Rσ** chirality C_σ stereoisomers for **E** field values of -25.0×10^{-4} a.u. and $+25.0 \times 10^{-4}$ a.u., in contrast to the behavior in the absence of an applied **E** field. Therefore, the effect of the **E** field = $\pm 25.0 \times 10^{-4}$ a.u. is to render the S_a and R_a geometric stereoisomers as comprising pure **Sσ** and pure **Rσ** chirality C_σ components, respectively. The values of $C_{\sigma mixing}$ are larger by at least a factor of two for values of the **E** field = -50.0×10^{-4} a.u and -100.0×10^{-4} a.u than for the oppositely directed **E** field, i.e., for **E** field = $+50.0 \times 10^{-4}$ a.u and $+100.0 \times 10^{-4}$ a.u. This indicates that $C_{\sigma mixing}$ is enhanced for the C3←O10 *BCP* bond path direction and reduced for the oppositely directed C3→O10 *BCP* bond path.

The value of $F_{\sigma mixing} = 0$ in the absence of an **E** field; however, the $F_{\sigma mixing}$ values are rather significant with the application of an **E** field. The presence of non-zero $F_{\sigma mixing}$ for the applied **E** fields can explain the reduction in the magnitude of the bond flexing $\sum F_\sigma$, i.e., an increase in the bond stiffness, indicated by the values of $F_{\sigma E} < 1$ in Table 2. $F_{\sigma mixing}$ remains unaffected by the **E** field direction, in contrast to $C_{\sigma mixing}$.

The values of $A_{\sigma mixing} = 0$ for all values of the applied **E** field, which corresponds to a complete lack of mixing of the **Sσ** and **Rσ** bond axiality A_σ components and is due to a lack of significant torsional C1-C2 *BCP* bond path curvature; see the Theoretical Background.

The effect of the ±**E** field on the chirality $\sum C_\sigma$, bond flexing $\sum F_\sigma$, and bond axiality $\sum A_\sigma$ is determined by $C_{\sigma E}$, $F_{\sigma E}$, and $A_{\sigma E}$, respectively, which correspond to the ratio of the values in the presence of the **E** field. The ratios of $C_{\sigma E}$, $F_{\sigma E}$, and $A_{\sigma E}$ are defined as the ratios $C_{\sigma E} = \sum C_\sigma / \sum C_\sigma |_{E=0}$, $F_{\sigma E} = \sum F_\sigma / \sum F_\sigma |_{E=0}$, and $A_{\sigma E} = \sum A_\sigma / \sum A_\sigma |_{E=0}$, respectively, as shown in Table 2.

We observe that the application of a -**E** field consistently reduces the values of $C_{\sigma E}$ compared with a +**E** field. The $C_{\sigma E}$ values increase with the magnitude of the +**E** field, with $C_{\sigma E} = 1.0456$ for +**E** field = $+100.0 \times 10^{-4}$ a.u and only just exceeding that of alanine in the absence of an **E** field. The effect of the **E** field on the bond flexing $F_{\sigma E}$ is very similar for the +**E** field and -**E** field in that both cause a significant decrease. The ±**E** field causes the bond axiality values $A_{\sigma E} > 1.0$ in all cases and $A_{\sigma E}$ exceeds 2.0 for +**E** field = $+100.0 \times 10^{-4}$ a.u.

The chirality-helicity values $C_{helicity E}$ all increase in the presence of the applied ±**E** field due to the induction of increases in $A_{\sigma E}$, where the increase is greater for the +**E** field values. The values of $A_{\sigma E}$ indicate a very significant enhancing interaction with the ±**E** field compared with $C_{\sigma E}$.

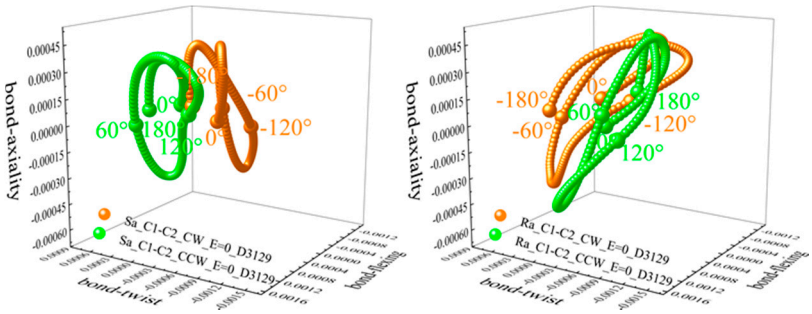

Figure 1. The stress tensor trajectory $T_\sigma(s)$ of the torsional C1-C2 *BCP* for the CW ($-90.0° \le \theta \le 0.0°$) and CCW ($0.0° \le \theta \le +90.0°$) directions corresponding to the D3129 dihedral angle for the **E** field = 0. Left panel: the S_a stereoisomer; Right panel: the R_a stereoisomer. The degree markers for the torsion θ are indicated at steps of 30.0°.

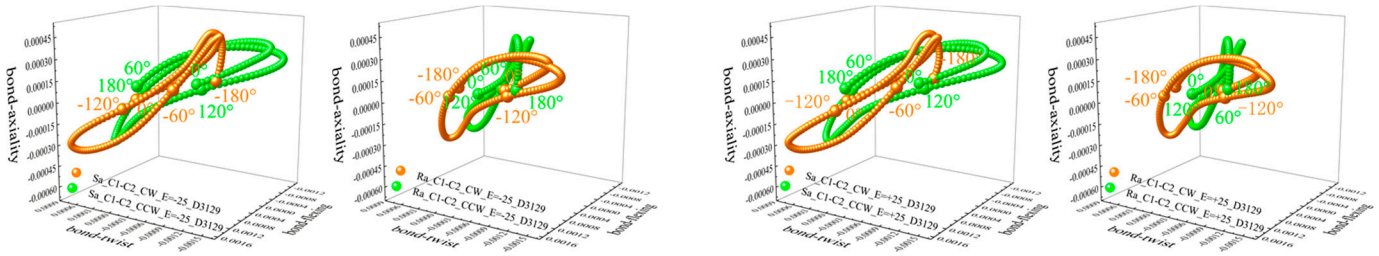

Figure 2. $T_\sigma(s)$ of the torsional C1-C2 *BCP* bond path for the **E** field = -25×10^{-4} a.u. (**a**) and $+25 \times 10^{-4}$ a.u. (**b**). $T_\sigma(s)$ of the S_a and R_a stereoisomers are presented in the left and right panels of (**a**,**b**), respectively; see also Figure 1.

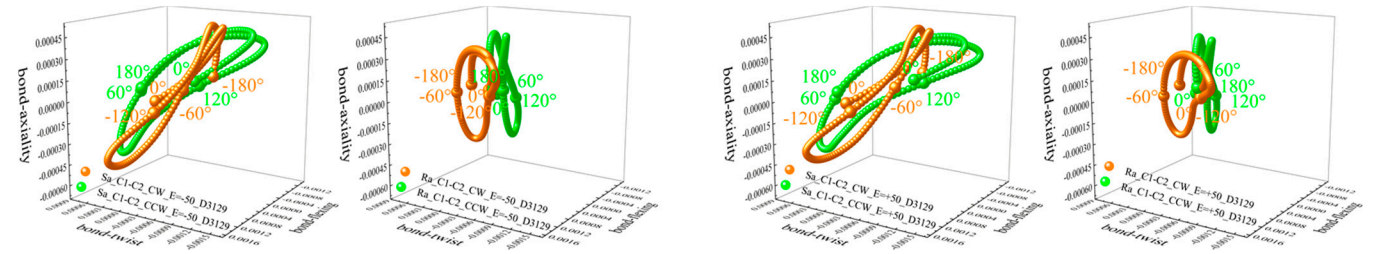

Figure 3. $T_\sigma(s)$ of the torsional C1-C2 *BCP* bond path for the **E** field = -50×10^{-4} a.u. (**a**) and $+50 \times 10^{-4}$ a.u. (**b**). $T_\sigma(s)$ of the S_a and R_a stereoisomers are presented in the left and right panels of (**a**,**b**), respectively; see also Figure 2.

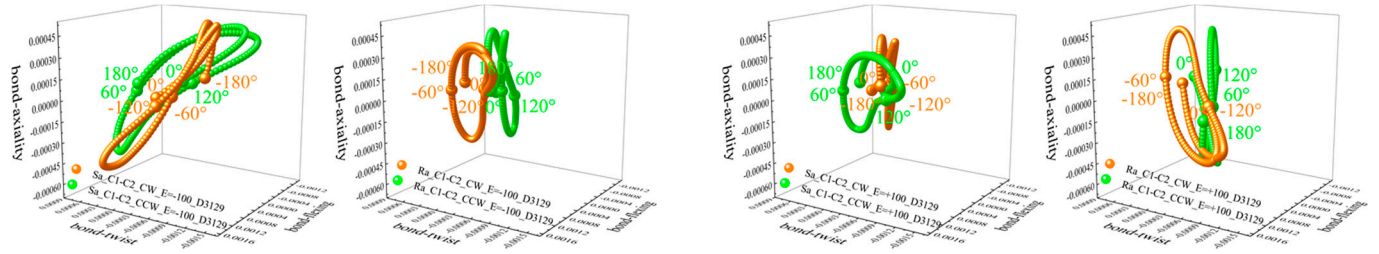

Figure 4. $T_\sigma(s)$ of C1-C2 *BCP* for the **E** field = -100×10^{-4} a.u. (**a**) and $+100 \times 10^{-4}$ a.u. (**b**); see also Figure 3.

4. Conclusions

In this NG-QTAIM investigation, we determined the effects of a non-structurally distorting **E** field on the S_a and R_a geometric stereoisomers of the alanine molecule using the recently introduced spanning $T_\sigma(s)$. We discovered that the values of the chirality-helicity $C_{helicity\mathbf{E}}$, the complete NG-QTAIM quantification of chirality, can be manipulated with an applied **E** field whilst reducing the structural strain in the form of the ratio of the bond flexing $F_{\sigma\mathbf{E}}$. We found that in the presence of the **E** field, a *mix* of $\mathbf{S}_\sigma$ and $\mathbf{R}_\sigma$ components, in all but one case, resulted in a reduction in the chirality $\sum C_\sigma$ and bond flexing $\sum F_\sigma$ but for none of the bond axiality values A_σ. The U_σ space $\mathbf{S}_\sigma$ and $\mathbf{R}_\sigma$ chirality stereoisomers were found to be in agreement with the CIP naming schemes for all ±**E** field values.

In all cases, the applied **E** field resulted in the ratio of the bond axiality values $A_{\sigma\mathbf{E}} > 1$ responding strongly due to the increased ease of the resultant C1-C2 *BCP* sliding. The complete absence of $\mathbf{S}_\sigma$ and $\mathbf{R}_\sigma$ bond axiality $A_{\sigma mixing}$ mixing for all values of the applied ±**E** field was due to a lack of significant torsional C1-C2 *BCP* bond path curvature. The lack of $A_{\sigma mixing}$ mixing for all values of the applied **E** field resulted in an increase in the chirality-helicity $C_{helicity}$ compared to the absence of the **E** field. Therefore, the large effect

on the ratio of the $A_{\sigma E}$ values due to the ±**E** field demonstrates that it is essential to account for $\sum A_{\sigma}$ for a complete understanding of the manipulation of chirality.

Values of $C_{\sigma mixing} > 0$ were found to indicate the presence of an achiral character in the range 2% to 7%, both in the absence and presence of the applied **E** field. A single instance of purely chiral alanine was found for an applied **E** field = $\pm 25 \times 10^{-4}$ a.u., corresponding to a value of $C_{\sigma mixing} = 0$, thus indicating a complete lack of achiral character. The quantification of mixing of the $\mathbf{S}_{\sigma}$ and $\mathbf{R}_{\sigma}$ components determined by $C_{\sigma mixing}$ is an additional feature provided by NG-QTAIM that enables the presence of achiral behaviors to be accounted for.

The magnitude of the ratio of the bond flexing $F_{\sigma E}$ decreased in the presence of all values of the applied **E** field. This finding indicates the significance of monitoring the **E** field magnitude and direction to minimize the bond flexing $\sum F_{\sigma}$ to achieve less destructive, i.e., bond flexing $F_{\sigma E}$, manipulation of the chirality $\sum C_{\sigma}$. A useful effect of tracking the changes in the U_{σ} space distortion sets $\sum\{C_{\sigma},F_{\sigma},A_{\sigma}\}$ was provided by the ability to choose ±**E** field values that increased or decreased $C_{helicity E}$ whilst reducing the unwanted outcome of bond flexing $\sum F_{\sigma}$ that occurred for **E** field = $+100.0 \times 10^{-4}$ a.u.

Future investigations using NG-QTAIM could include manipulation of the components of the U_{σ} space distortion sets $\sum\{C_{\sigma},F_{\sigma},A_{\sigma}\}$ using a pair of left and right circularly-polarized laser pulses. This has the benefit of not requiring the geometric C1-C2 *BCP* torsions that are used to create the spanning stress tensor trajectories $T_{\sigma}(s)$. The application of non-ionizing ultra-fast laser irradiation that would be fast enough to avoid disrupting atomic positions would enable non-destructive manipulation, i.e., increasing or decreasing the ratio of the chirality $C_{\sigma E}$ and bond axiality $A_{\sigma E}$ whilst monitoring the degree of bond flexing $F_{\sigma E}$. NG-QTAIM could consequently open up a wide scientific field for chiral solid-state and molecular systems to track, control, and quantify the chirality of a wide range of molecular devices, including photochromic switches [25] and azobenzene chiroptical switches [26]. In addition, the design of chiral-optical molecular rotary motors [27] that use synthetic controllable chiral light for ultrafast imaging of chiral dynamics in gases [28] could be investigated with NG-QTAIM.

Supplementary Materials: The following supporting information can be downloaded at: https://www.mdpi.com/article/10.3390/sym14102075/s1, **Supplementary Materials S1.** NG-QTAIM and stress tensor theoretical background and procedure to generate the stress tensor trajectories $T_{\sigma}(s)$. **Supplementary Materials S2.** Distance measures for alanine with and without an applied electric field. **Supplementary Materials S3.** Scalar measures with for alanine with and without an applied electric field. **Supplementary Materials S4.** Additional $T_{\sigma}(s)$ and tables of the alanine torsional C1-C2 *BCPs.*

Author Contributions: Methodology, S.J.; software, S.R.K.; formal analysis, Z.L. and Y.P.; investigation, S.J.; resources, S.J.; data curation, W.Y., X.F. and Z.L.; writing—original draft preparation, S.J.; writing—review and editing, H.F. and T.v.M. ; visualization, W.Y.; supervision, T.X. and S.R.K.; project administration, S.J.; funding acquisition, S.J. All authors have read and agreed to the published version of the manuscript.

Funding: The Hunan Natural Science Foundation of China project approval number: 2022JJ30029. The One Hundred Talents Foundation of Hunan Province is also gratefully acknowledged for the support of S.J. and S.R.K. H.F. and T.v.M. gratefully acknowledge computational support via the EaStCHEM Research Computing Facility.

Data Availability Statement: Data available on reasonable request.

Conflicts of Interest: The authors declare no conflict of interest.

References

1. Castiglioni, E.; Abbate, S.; Longhi, G. Experimental Methods for Measuring Optical Rotatory Dispersion: Survey and Outlook. *Chirality* **2011**, *23*, 711–716. https://doi.org/10.1002/chir.20981.
2. Xu, T.; Li, J.H.; Momen, R.; Huang, W.J.; Kirk, S.R.; Shigeta, Y.; Jenkins, S. Chirality-Helicity Equivalence in the S and R Stereoisomers: A Theoretical Insight. *J. Am. Chem. Soc.* **2019**, *141*, 5497–5503. https://doi.org/10.1021/jacs.9b00823.

3. Wang, D.Z. A Helix Theory for Molecular Chirality and Chiral Interaction. *Mendeleev Commun.* **2004**, *14*, 244–247. https://doi.org/10.1070/MC2004v014n06ABEH002051.
4. Beaulieu, S.; Comby, A.; Descamps, D.; Fabre, B.; Garcia, G.A.; Géneaux, R.; Harvey, A.G.; Légaré, F.; Mašín, Z.; Nahon, L.; et al. Photoexcitation Circular Dichroism in Chiral Molecules. *Nat. Phys.* **2018**, *14*, 484–489. https://doi.org/10.1038/s41567-017-0038-z.
5. Harper, K.C.; Sigman, M.S. Three-Dimensional Correlation of Steric and Electronic Free Energy Relationships Guides Asymmetric Propargylation. *Science* **2011**, *333*, 1875–1878. https://doi.org/10.1126/science.1206997.
6. Garner, M.H.; Corminboeuf, C. Helical Electronic Transitions of Spiroconjugated Molecules. *Chem. Commun.* **2021**, *57*, 6408–6411. https://doi.org/10.1039/D1CC01904J.
7. Xing, H.; Azizi, A.; Momen, R.; Xu, T.; Kirk, S.R.; Jenkins, S. Chirality–Helicity of Cumulenes: A Non-Scalar Charge Density Derived Perspective. *Int. J. Quantum Chem.* **2022**, *122*, e26884. https://doi.org/10.1002/qua.26884.
8. Kirk, S.R.; Jenkins, S. Beyond Energetic and Scalar Measures: Next Generation Quantum Theory of Atoms in Molecules. *WIREs Comput. Mol. Sci.* **2022**, *Early View*, e1611. https://doi.org/10.1002/wcms.1611.
9. Hanson, R.M.; Musacchio, S.; Mayfield, J.W.; Vainio, M.J.; Yerin, A.; Redkin, D. Algorithmic Analysis of Cahn–Ingold–Prelog Rules of Stereochemistry: Proposals for Revised Rules and a Guide for Machine Implementation. *J. Chem. Inf. Model.* **2018**, *58*, 1755–1765. https://doi.org/10.1021/acs.jcim.8b00324.
10. Nie, X.; Yang, Y.; Xu, T.; Biczysko, M.; Kirk, S.R.; Jenkins, S. The Chirality of Isotopomers of Glycine Compared Using Next-Generation QTAIM. *Int. J. Quantum. Chem.* **2022**, *122*, e26917. https://doi.org/10.1002/qua.26917.
11. Li, Z.; Xu, T.; Früchtl, H.; van Mourik, T.; Kirk, S.R.; Jenkins, S. Mixed Chiral and Achiral Character in Substituted Ethane: A Next Generation QTAIM Perspective. *Chem. Phys. Lett.* **2022**, *803*, 139762.
12. Li, Z.; Xu, T.; Früchtl, H.; van Mourik, T.; Kirk, S.R.; Jenkins, S. Chiral and Steric Effects in Ethane: A next Generation QTAIM Interpretation. *Chem. Phys. Lett.* **2022**, *800*, 139669. https://doi.org/10.1016/j.cplett.2022.139669.
13. Shaik, S.; Danovich, D.; Joy, J.; Wang, Z.; Stuyver, T. Electric-Field Mediated Chemistry: Uncovering and Exploiting the Potential of (Oriented) Electric Fields to Exert Chemical Catalysis and Reaction Control. *J. Am. Chem. Soc.* **2020**, *142*, 12551–12562. https://doi.org/10.1021/jacs.0c05128.
14. Li, Z.; Nie, X.; Xu, T.; Li, S.; Yang, Y.; Früchtl, H.; van Mourik, T.; Kirk, S.R.; Paterson, M.J.; Shigeta, Y.; et al. Control of Chirality, Bond Flexing and Anharmonicity in an Electric Field. *Int. J. Quantum. Chem.* **2021**, *121*, e26793. https://doi.org/10.1002/qua.26793.
15. Wolk, J.L.; Hoz, S. Inducing Chirality Ex Nihilo by an Electric Field. *Can. J. Chem.* **2014**, *93*, 459–462. https://doi.org/10.1139/cjc-2014-0354.
16. Bader, R.F.W. Quantum Topology of Molecular Charge Distributions. III. The Mechanics of an Atom in a Molecule. *J. Chem. Phys.* **1980**, *73*, 2871–2883. https://doi.org/10.1063/1.440457.
17. Anderson, J.S.M.; Ayers, P.W.; Hernandez, J.I.R. How Ambiguous Is the Local Kinetic Energy? *J. Phys. Chem. A* **2010**, *114*, 8884–8895. https://doi.org/10.1021/jp1029745.
18. Anderson, J.S.M.; Ayers, P.W. Quantum Theory of Atoms in Molecules: Results for the SR-ZORA Hamiltonian. *J. Phys. Chem. A* **2011**, *115*, 13001–13006. https://doi.org/10.1021/jp204558n.
19. Keith, T.A. *AIMAll (19.10.12)*; TK Gristmill Software: Overland Park, KS, USA, 2019; Available online: Http://Aim.Tkgristmill.Com (accessed on 1 October 2022).
20. Xu, T.; Kirk, S.R.; Jenkins, S. A Comparison of QTAIM and the Stress Tensor for Chirality-Helicity Equivalence in S and R Stereoisomers. *Chem. Phys. Lett.* **2020**, *738*, 136907. https://doi.org/10.1016/j.cplett.2019.136907.
21. Szarek, P.; Sueda, Y.; Tachibana, A. Electronic Stress Tensor Description of Chemical Bonds Using Nonclassical Bond Order Concept. *J. Chem. Phys.* **2008**, *129*, 094102. https://doi.org/10.1063/1.2973634.
22. Tian, T.; Xu, T.; Kirk, S.R.; Rongde, I.T.; Tan, Y.B.; Manzhos, S.; Shigeta, Y.; Jenkins, S. Intramolecular Mode Coupling of the Isotopomers of Water: A Non-Scalar Charge Density-Derived Perspective. *Phys. Chem. Chem. Phys.* **2020**, *22*, 2509–2520. https://doi.org/10.1039/C9CP05879F.
23. Frisch, M. J.; Trucks, G. W.; Schlegel, H. B.; Scuseria, G. E.; Robb, M. A.; Cheeseman, J. R.; Scalmani, G.; Barone, V.; Mennucci, B.; Petersson, G. A.; et al. Gaussian 09, Revision E.01. Inc., Wallingford CT:, USA, 2009.
24. Kirk, S.R.; Jenkins, S. QuantVec. Available online: Https://Doi.Org/10.5281/Zenodo.5553686 (accessed on 1 October 2022).
25. de Jong, J.J.D.; van Rijn, P.; Tiemersma-Wegeman, T.D.; Lucas, L.N.; Browne, W.R.; Kellogg, R.M.; Uchida, K.; van Esch, J.H.; Feringa, B.L. Dynamic Chirality, Chirality Transfer and Aggregation Behaviour of Dithienylethene Switches. *Tetrahedron* **2008**, *64*, 8324–8335. https://doi.org/10.1016/j.tet.2008.05.129.
26. Weingart, O.; Lan, Z.; Koslowski, A.; Thiel, W. Chiral Pathways and Periodic Decay in Cis-Azobenzene Photodynamics. *J. Phys. Chem. Lett.* **2011**, *2*, 1506–1509. https://doi.org/10.1021/jz200474g.
27. Nikiforov, A.; Gamez, J.A.; Thiel, W.; Filatov, M. Computational Design of a Family of Light-Driven Rotary Molecular Motors with Improved Quantum Efficiency. *J. Phys. Chem. Lett.* **2016**, *7*, 105–110. https://doi.org/10.1021/acs.jpclett.5b02575.
28. Ayuso, D.; Neufeld, O.; Ordonez, A.F.; Decleva, P.; Lerner, G.; Cohen, O.; Ivanov, M.; Smirnova, O. Synthetic Chiral Light for Efficient Control of Chiral Light–Matter Interaction. *Nat. Photonics* **2019**, *13*, 866–871. https://doi.org/10.1038/s41566-019-0531-2.